Doppler Ultrasound Systems Designed for Tumor Blood Flow Imaging

Christian Kargel, *Member, IEEE*, Gernot Plevnik, Birgit Trummer, and Michael F. Insana, *Member, IEEE*

***Abstract*—There is a great need for adaptable instrumentation for imaging the volume and dynamics of flowing blood in cancerous lesions. Applications include basic biological research and clinical diagnosis. Commercial instruments are not currently optimized for such applications and system modification for research is difficult if at all possible. This paper describes a laboratory instrument for developing tumor imaging techniques. It compares common and improved estimators through a detailed error analysis of simulated and experimental echo data. Broadband power-Doppler imaging with contrast media is found to be ideal for visualizing the volume of moving blood. The two-dimensional autocorrelator in color-flow imaging for time-resolved velocity estimation provides unbiased estimates and is reasonably efficient for broadband echoes. Ultrasonic blood flow imaging can be sensitive for tumor imaging if the instrumentation and algorithms are optimized specifically for the experimental conditions.**

***Index Terms*—Autocorrelator, blood velocity estimation, color-flow imaging, error estimation, flow phantom, power Doppler, tumors.**

I. Introduction

SPATIAL PATTERNS and dynamics of blood flow are primary factors determining the growth and development of metastatic tumors. There is evidence suggesting that blood flow features can predict the metastatic potential of breast lesions. Consequently, flow and perfusion imaging could play essential roles in the management and treatment of breast cancer. For example, microvessel density within regions of intense neovascularization (INV) in invasive breast carcinoma has been found to be a significant prognostic indicator for overall and relapse-free survival in patients with early-stage breast carcinoma [1], [2]. Other investigators, however, concluded that vessel density was not predictive of metastasis-free survival or overall survival [3], [4], while still others found significant correlations between INV vessel density and survival in axillary lymph node metastases of patients but not in the primary lesion [5]. These discrepancies may be resolved, in part, through a clearer understanding of the limits of in vivo imaging technologies applied specifically to this diagnostic problem.

Manuscript received July 11, 2002; revised December 17, 2003. This work was supported by NIH.

Ch. Kargel is with the Department of Biomedical Engineering, University of California, Davis CA 95616 USA and also with the Carinthia Tech Institute, University of Applied Sciences, Austria (e-mail: c.kargel@cti.ac.at).

G. Plevnik, B. Trummer, and M. F. Insana are with the Department of Biomedical Engineering, University of California, Davis CA 95616 USA (e-mail: mfinsana@ucdavis.edu).

Digital Object Identifier 10.1109/TIM.2004.823296

Numerous investigators have found ultrasonic techniques, particularly power Doppler imaging and associated parameters, are able to describe microvessel density, indicate INV regions, and differentiate benign and malignant masses [6]–[8]. The hypothesis is that the spatial and temporal tumor flow patterns reliably indicate malignant potential and therapeutic response. Clinical reliability of this indicator depends on understanding limitations of the instrumentation and parametric estimators. Unlike the conditions for blood velocity estimation in large vessels, where pulsed Doppler ultrasound is widely applied, tumor blood flow patterns are spatially disorganzied and heterogeneous on the scale of the Doppler pulse volume. Vessels produced during angiogenesis are small and tortuous such that the net red blood cell (RBC) velocity vector, summed over the pulse volume, is small even when perfusion is high. The low Doppler frequency and characteristically weak scattering amplitude combine to yield a very low signal-to-noise ratio (SNR) for velocity estimates in tumors. Low Doppler frequencies exacerbate efforts to filter clutter from the surrounding tissues that move at the same velocity as the RBCs.

To optimize system performance, it is essential to perform an analysis of instrumentation errors that are experienced under common tumor blood flow conditions. That is the purpose of this paper. Only then can we understand measurement limitations and improve the system design. We summarize essential instrumentation design features of a Doppler instrument by describing our laboratory system built for imaging tumor blood flow in small animals. We also describe an improved velocity estimator based on the Kasai autocorrelator and evaluate measurement errors under slow-flow conditions using a tissue-like flow phantom.

II. System Design

The pulse-echo imaging system diagrammed in Fig. 1 was assembled. Five mechanically scanned axes position single-element or annular array transducers. Mechanical scanning compromises frame rate to provide maximum flexibility for data acquisition and echo processing. B-mode image acquisitions for 20×20 mm^2 regions are possible at 1 frame per second with negligible positional jitter. Although color M-mode and spectral Doppler acquisitions are straightforward, color flow imaging is achievable only with gated acquisition. Acquisition, processing, and display are coordinated in Labview.

A programmable motion controller (Galil, Inc., DMC2000) determines the position of the ultrasound transducer along 3 cartesian axes of the micro-positioning unit (Parker-Daedal). Optical quadrature encoders provide an absolute position ac-

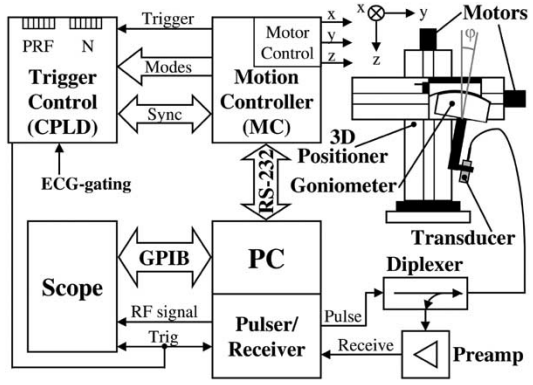

Fig. 1. Block diagram of the ultrasound scanner.

curacy of 100 nm. The remaining two degrees of freedom are applied to manually tilt the transducer about the z axis. Fixtures precisely hold a variety of single element transducers and an annular array. Transducers are driven by a software-controlled tone-burst pulser/receiver (Matec, Inc., TB1000). A low-noise pre-amplifier (Mitec, $\mathrm{NF} = 1.2$ dB, $\mathrm{gain} = 30$ dB) improves echo SNR and a diplexer (Matec, DIP 3) protects the pre-amplifier from the high-voltage transmit pulses, as shown in Fig. 1. To use our eight-ring annular array, we add a home-built low-noise multiplexer and seven additional diplexers as described in [9]. The timing and switch pattern of the multiplexer are set by a software-controlled high-speed digital I/O card (National Instruments, DIO-32HS). RF echo signals are recorded at 8 bits and sampling rates up to 8 GS/s by a digital oscilloscope (LeCroy, WavePro 940) with 16 MByte acquisition memory.

Communication with the digital motion controller, scan action, control of the pulser/receiver and oscilloscope, synchronization data acquisition and transfer, signal and image processing as well as image display are carried out by a host PC running LabView using IMAQ-Vision software tools. IMAQ-Vision was originally designed to take advantage of Intel's MMX technology with no need for RISC processors. MMX accelerates integer or fixed-point functions that are used to process 8-bit data. Computational performance gains of 400% over standard processors are obtained for many common functions [10].

A. Acquisition and Display Modes

Three data acquisition modes are implemented: M-mode (motion) records data over time at a fixed spatial position, S-mode (swept scan) records echo data as a function of time while slowly translating the transducer perpendicular to the beam axis [11] to acquire data from several spatial locations, and gated R-mode (repetition) combines full temporal and spatial acquisition for repetitive physiological signals. All three acquisition modes can be applied to several display modes: standard B-mode (echo amplitude brightness), strain imaging, and velocity imaging, the latter includes color M-mode, color flow (CF), and power Doppler (PD) [12], [13]. Display frame rates in S- and R-mode are mostly determined by the scan duration whereas in M-mode, only data transfer time and computational load are important. The display mode and experimental situation determine the acquisition mode. For example, in S-mode only one ultrasound pulse transmission and echo recording per line-of-sight (LOS) and a single scan of the region of interest (ROI) are required to produce a standard B-mode image. One pulse per LOS and two or more sequential scans of the same ROI are required for strain imaging [14]. Two or more pulses per LOS and one scan are required to generate CF images. If the blood speed is "high," M-mode or gated R-mode acquisitions for mechanically scanned instruments are needed to avoid spatial aliasing. If the blood speed is "low," S-mode acquisition may be selected to provide more spatial information (high and low speeds are defined below). Combining B-mode imaging and velocity estimation to form CF and PD images, or combining strain and velocity estimates for strain-flow imaging [15], we must also be able to vary the transmitted pulse bandwidth. Precise velocity estimates are obtained with narrowband transmission, whereas B-mode and strain imaging demand broadband pulses. Pulse duration is varied by software control for interleaved data acquisition. Under conditions of poor echo SNR, the number of transmitted pulses per LOS, N (also referred to as "packet size" or "ensemble length"), can be as high as 20. Thus noise is reduced at the expense of frame rate due to longer data transfer and computational times.

In *M-mode* acquisition, the transducer is stationary over a LOS selected from a scout B-mode image. The pulser/receiver drives the transducer at a pulse repetition frequency (PRF) f_{PRF} determined by an internal, software-adjustable clock frequency.

In *S-mode* acquisition, the transducer is scanned continuously and rectilinearly in the xy plane of Fig. 1 while firing pulses and recording corresponding echo signals one round trip time later. Since the speed of sound in soft tissues, 1540 m/s, is much higher than the typical mechanical scan speed of 0.020 m/s, no additional restrictions are placed on spatial resolution or frame rate. A key feature of the Galil DMC2000 motion controller/optical encoder combination is the ability to deliver TTL impulses that precisely define the transducer position. Galil, Inc., guarantees output impulses within a maximum delay time of 100 ns after specified positions have been reached. Hence, at a scan speed of 20 mm/s, the positional error is less than 2 nm.

Constant transducer scan speed is preferred to ensure that positioning accuracy and data acquisition are not influenced by acceleration. Position and scan speed fluctuations are determined by the parameters of a PID controller resident in the DMC2000 that must be optimized for specific situations. After optimization we calculated the velocity mean and standard deviation for a nominal scan speed of 4 mm/s over a 60 mm path where the distance and speed were recorded every 5 ms. Using an air-dampened optical table to minimize environmental vibrations, we measured the average speed and standard deviation to be 4.0002 ± 0.0216 mm/s. This standard deviation is approximately constant up to a scan speed of 20 mm/s, suggesting the system has a noise floor.

Unfortunately, at scan speeds >5 mm/s, most commercial motion controllers are unable to generate the output triggering necessary for CF imaging: a certain number N of trigger impulses with predefined f_{PRF} at pre-set spatial locations is

required.[1] At higher scan speeds, impulse output becomes unstable depending on the desired PRF and Δs, the distance traveled between successive firings. When using a standard DMC2000 to generate the necessary CF pulsing strategy, the PRF for acceptable Δs is limited to about 500 Hz [16]. This problem can be avoided by either increasing Δs to give the MC more time to react or firing single ultrasound pulses instead of pulse packets. This might, however, result in inappropriate spatial sampling due to spatial aliasing or a spatial separation between pulse packets that equals their interspatial distance.

Additional disadvantages lessen enthusiasm for these solutions. First, for a given packet size, the minimum detectable blood velocity in S-mode is higher than that for M-mode. This is because increasing Δs reduces the correlation between adjacent echo signals and thus increases the flow velocity variance. Second, the PRF is a function of both the scan speed and Δs. In order to maintain a constant PRF at higher scan speeds, Δs must be adjusted accordingly to higher values, which further reduces coherence between echo signals from adjacent LOS. Third, to maintain the constant temporal sampling interval (constant PRF) required in subsequent signal processing, the scan velocity must also be constant, which does not allow the system to adapt to the imaging tasks.

To overcome these limitations, we developed a digital trigger control based on a programmable logic device (Xilinx, CPLD XC 9572, 40 MHz, 1600 gates) that produces TTL impulse packets between 1 and 32 at 80 Hz $\leq f_{\mathrm{PRF}} \leq$ 15 kHz after the DMC2000 motion controller has generated a single TTL output impulse at a particular spatial location. The trigger control (Fig. 1) uncouples the choices of scan speed and PRF. The only remaining restriction on the PRF for a given scan speed is that the entire echo pulse packet must be received before further impulse packets are released at subsequent LOS.

R-mode gated acquisition is required when the mechanical scan speed is too slow to image flow dynamics over a large ROI. Electronic scanning using linear or phased array technology is the best solution but currently only available in proprietary commercial ultrasound systems. Pulsed blood flow is sufficiently periodic to acquire data from individual repetitions at a preset phase from different spatial locations. Overall system synchronization is handled by the CPLD trigger control which provides the necessary ECG-gating input. ECG-triggering can also be activated for M-mode acquisition.

B. Resolution

Circular aperture transducers produce an axisymmetric sample volume for velocity estimation that determines the echo signal at any instant of time. The sample volume is characterized by the range and cross-range resolutions given by the pulse dimensions along the z axis and in the xy plane, respectively, in Fig. 2. For all display modes, it is critical to minimize the sample volume (maximize resolution). However, for strain and velocity estimation it is particularly important to be able to match beam properties according to the imaging task. Displacement gradients (strains) on the scale smaller than the sample volume result in large velocity and strain estimation errors because of the loss of signal coherence required for correlation-based estimators [14].

[1]The related hardware must be armed and reset by the motion controller software. Although this action can be programmed in a second thread, the maximum scan speed for CF imaging using the DMC 2000 is limited to approximately 5 mm/s, often requiring R-mode acquisition.

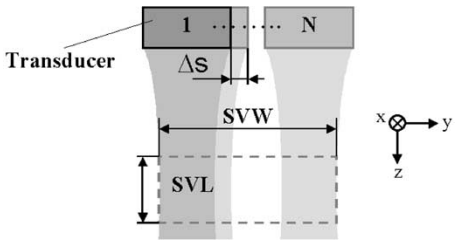

Fig. 2. Illustration of resolution concepts for color flow imaging.

1) Range Resolution: Range resolution for velocity estimation is the minimum range separation of two scatterers traveling at different velocities that can be estimated as distinct velocities. Of the many features that affect range velocity resolution, the sample volume length is most important (Fig. 2). The sample volume length (SVL) in a medium with sound speed c is simply

$$\mathrm{SVL} = \frac{c}{2}(T_p + T_g). \tag{1}$$

When rectangular-shaped ultrasound pulses and rectangular range gates are applied, the pulse duration T_p and range gate duration T_g are straightforward. For more general pulse and gating functions, the full-width-at-half-maximum (FWHM or -6 dB) concept and the effective duration concept [17], e.g.

$$T_p = T \sum_{m=-\infty}^{\infty} \frac{|h_p[mT]|}{|h_p|^{\max}}. \tag{2}$$

can be applied to find T_p and T_g. In (2), $h_p[mT]$ is the (real) pulse-echo impulse response, $|h_p|^{\max}$ is the maximum absolute value, and T is the temporal sampling interval.

2) Cross-Range Resolution: Cross-range resolution depends primarily on the sample volume width (SVW) as illustrated in Fig. 2. In the scan plane (yz plane), SVW is determined by the pulse-echo beam width (BW), scan speed and PRF

$$\mathrm{SVW} = (N-1)\Delta s + \mathrm{BW}. \tag{3}$$

The transducer displacement increment is Δs = scan speed/f_{PRF}. The out-of-plane (x axis) sample volume dimension is given by the beam width. At the focal length z_f of a focused piston radiator of diameter D and at wavelength λ_0, the FWHM beam width is approximately BW $= \lambda_0 \times f/\#$, where the f-number is $f/\# = z_f/D$.

3) Detectable Velocities: It is well known that the PRF for pulsed Doppler is bounded by the maximum tissue depth z_m and sound speed c such that $f_{\mathrm{PRF}} \leq c/2z_m$. For measurements free of temporal aliasing, the PRF must exceed

$$f_{\mathrm{PRF}} > \frac{4f_0 \cdot \left(1 + \frac{B}{2}\right) v_m \cos\theta}{c} \tag{4}$$

with the transmitted carrier frequency f_0, fractional echo bandwidth B, Doppler angle θ and maximum blood velocity v_m in the sample volume [12]. For example, a 10 MHz transducer focused at $f/2(f/\# = 2)$ in soft biological tissue $(c = 1540\,\mathrm{m/s})$ has a beam width of 0.31 mm. For $z_f = 50$ mm and a tumor diameter of 10 mm, the largest PRF possible is $c/(2 \cdot 0.055\,\mathrm{m}) = 14$ kHz. However, the highest PRF our pulser can provide is just 4 kHz, which means given that $\theta \leq 60°$ the *maximum detectable velocity* our system can measure is $\sim$300 mm/s, on the order of aortic velocities. For a scan speed of 20 mm/s and $f_{\mathrm{PRF}} = 4$ kHz, $\Delta s = 0.005$ mm and from (3) with $N = 8$, we find SVW $\simeq 0.34$ mm. This value is only slightly larger than the beam width. Since $\Delta s < 0.02$BW, there is very little echo decorrelation even at that this high scan speed.

At the other end of the physiological spectrum, RBC velocities in tumor capillaries are about 5 mm/s. This relatively low value allows a decrease in PRF to reduce the I/O and computational loads without introducing aliasing. The minimum acceptable PRF can be found from (4) for a relatively narrow fractional bandwidth $B = 0.2$ to be just 72 Hz and the lowest PRF possible with our pulser is 80 Hz. However, maintaining a scan speed of 20 mm/s means that Δs increases such that $\Delta s \simeq$ BW, which leads to prohibitively large echo decorrelation. We compromise and choose a higher PRF, often 500 Hz, and we reduce the scan speed to 5 mm/s for S-scan acquisition of slow flow. These parameters yield high echo coherence since $\Delta s \simeq 0.03$BW.

The *minimum detectable velocity* ultimately depends on the noise and clutter spectra relative to the blood spectrum as well as on measurement parameters. Clutter suppression is particularly difficult in slow-flow situations because the Doppler spectrum from weakly scattering RBCs overlaps that from strongly scattering surrounding tissues. Novel approaches to clutter filtering are currently receiving much attention [15], [18], [19]. Assuming clutter has been removed, the packet size N is the experimental parameter that determines the minimum measurable frequency, and therefore velocity, using Fourier-based Doppler spectrum estimation. The frequency increment for sampled echo signals is given by $\Delta f = 1/(NT_{\mathrm{PRF}})$ [21]. The sampling interval for pulsed Doppler measurements is $T_{\mathrm{PRF}} = 1/f_{\mathrm{PRF}}$. Therefore, the minimum measurable frequency is f_{PRF}/N. The lowest possible PRF using the TB1000 pulser is 80 Hz. Assuming $N = 8$, the lowest detectable frequency is 10 Hz which corresponds to a velocity of 0.77 mm/s ($c = 1540$ m/s, $f_0 = 10$ MHz, $\theta = 0$) where the aliasing velocity equals 3.1 mm/s. An increase to $N = 16$ spans the velocity range from 0.385 to 3.1 mm/s but lengthens the SVW and reduces the CF frame rate.

In M-mode, frame rate is not an issue. N can be enlarged and, for time-steady flow, is limited solely by the available acquisition memory of our oscilloscope. Provided that 2000 RF echo signals can be recorded (each of the signals is 64 μs long and sampled at 125 MS/s) at a PRF of 80 Hz, the minimum frequency becomes 0.04 Hz which corresponds to a velocity in the μm/s range (with an aliasing velocity of still 3.1 mm/s). Noise prevents us from estimating such low values in practice.

Consequently, if we can achieve sufficient echo SNR and suppress clutter, our system can measure the full range of blood velocities, from the aorta to capillaries. The maximum velocity is approximately 300 mm/s and the minimum can be less than 1 mm/s depending on the nature of the flow and the frame rate required. Our highest frame rate is far below commercial electronically-scanned systems, yet this instrument provides significantly more flexibility for research at lower cost. The minimum frequency/velocity limitation described above is not fundamental. It is possible to estimate phase shifts much smaller than π from signals shorter than $\lambda/2$. Examples are discussed in Section III below.

C. Noise Minimization and Optimized Filter Receiver

Blood flow estimation is ultimately limited by system noise. Three steps are implemented to maximize the echo SNR. First, a low-noise amplifier (LNA) with noise figure NF $= 1.2$ dB and 30-dB gain is applied prior to the receiver amplifier of the TB1000 to keep the overall noise figure (NF) small.[2] According to the well-known Friis formula [20], the contribution made by a given stage of cascaded and matched system elements to the overall system noise is the noise temperature of that stage divided by the total gain leading up to that stage. To minimize the overall system NF, the first stage (LNA) must have a low noise temperature and high gain. Since the output signal power is due only to the signal entering the input of each stage, while the output noise power is due to both input noise and noise internally generated, we wish to match impedances between all system elements. To maximize signal power, we normally need to use a receiver matched to the source. More precisely, the receiver input impedance should be tuned for maximum output SNR, a condition usually close to that of an input impedance match. Whenever the impedance of our system elements is not matched to the standard value of 50 Ω, we use additional matching devices.

Second, we apply analog passive RF bandbass filters of fourth order that also act as anti-aliasing filters over a relatively large bandwidth (e.g., from 10 to 20 MHz for a 15-MHz transducer). Broadband signals necessary for high resolution B-mode and strain imaging must also pass these filters without large attenuation.

Third, after digitizing the RF echo signals and quadrature down-mixing to baseband, we pass IQ signals through a digital six-pole lowpass filter. Butterworth characteristic was chosen because of its flat bandpass response. However, any kind of phase-shift sensitive measurement essentially demands a filter response with constant group delay. The best way of approximately achieving this goal in the analog domain is a filter with Bessel characteristic. In the digital domain, FIR filters are most often chosen over IIR filters because an exactly linear phase property can be implemented with FIR filters. In general, linear phase filters produce a constant time shift that can be counteracted by designing zero phase filters, which also have the desired property of not distorting the input signal's phase spectrum.

[2] NF $= 10 * \log_{10}(F) = 1.2$ dB where F is the noise factor defined by $F = 1 + T_n/T_0$. T_n is the noise temperature which has a value of 92.3 K for our LNA, and T_0 is the standard temperature, usually 290 K.

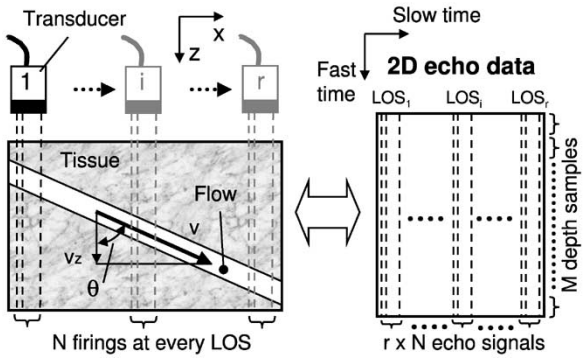

Fig. 3. Acquisition in S-mode (left) and the $M \times rN$-dimension matrix representation of echo data (right). M-mode acquisition is similar except the transducer does not move and $r = 1$.

Since our digital filter is run "off-line," the entire data sequence is available prior to filtering. This allows a noncausal, zero-phase filtering approach that eliminates the nonlinear phase distortion of our IIR LP filter with Butterworth characteristic [21]. The corner frequency of this baseband filter is set to half the RF echo signal bandwidth.

III. Flow Velocity Estimation

Like most commercial color-flow imaging systems, we use a phase domain velocity estimation technique known as the Kasai autocorrelator [22] because of its computational efficiency. Other velocity estimators, e.g., time-domain cross-correlation, two-dimensional (2-D) Fourier transform, maximum-likelihood and maximum entropy estimators, may exhibit superior performance to the autocorrelator but also have significantly greater computational requirements. In this section, we focus on two autocorrelation techniques for color-flow (CF), color-M-mode, and power Doppler (PD) imaging. Echo signal samples are organized in 2-D arrays for processing, where the terms "fast time" (columns) and "slow time" (rows) define the direction of the beam axis (RF sampling, index m) and pulse packet dimension (PRF sampling, index n), respectively. The situation is depicted in Fig. 3. Provided that scatterers move with velocity $\vec{v}$, the mean Doppler frequency computed along the slow-time direction is $f_D = f_0 2v_z/c$ where $v_z = |\vec{v}|\cos\theta$ is the axial velocity component.

A. One-Dimensional (1-D) Autocorrelator

The Kasai autocorrelator measures v_z by estimating the average phase shifts with respect to the central frequency of the transmitted pulses between consecutive echo signals in slow time for given depth locations along the fast-time axis. It is one-dimensional (1-D) in the sense that estimation occurs along the slow-time axis. The autocorrelator is able to provide estimates of the mean Doppler frequency in the time domain because of a relationship between spectral moments and autocorrelation derivatives [23]. v_z is proportional to the phase of the complex 2-D autocorrelation function $R(k,\ell)$ with lags $k = 0$ in fast-time and $\ell = 1$ in slow-time direction [22]

$$v_z = \frac{c}{2}\frac{f_{\mathrm{PRF}}}{2\pi f_0}\arctan\left(\frac{\Im[\hat{R}(0,1)]}{\Re[\hat{R}(0,1)]}\right) \tag{5}$$

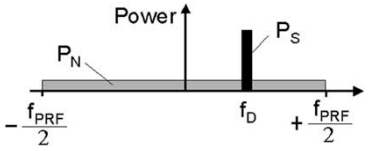

Fig. 4. Illustration of signal and white noise spectra with power P_S and P_N, respectively.

where $\Re$ and $\Im$ denote the real and imaginary parts. Other parameters were defined earlier. The correlation lag in seconds is calculated in slow-time from ℓT_{PRF} and in fast-time from kT, where T_{PRF} and T are, respectively, the slow- and fast-time sampling intervals. $\hat{R}(k,\ell)$ is an estimate of the complex correlation function computed from the in-phase $I(m,n)$ and quadrature-phase $Q(m,n)$ components of the baseband echo data

$$\hat{R}(k,\ell) = \sum_{m=0}^{M-k-1}\sum_{n=0}^{N-\ell-1}[I(m,n)+jQ(m,n)] \cdot[I(m+k,n+\ell)-jQ(m+k,n+\ell)]. \tag{6}$$

$N-1$ is the number of waveform pairs averaged to improve the estimation of $\hat{R}(k,\ell)$.

When the blood component of the Doppler spectrum is symmetric about its mean frequency, the autocorrelator yields unbiased estimates. However, in practice, the bias for asymmetric spectra is negligible for moderate spectral widths [24]. Unlike spectral estimators, autocorrelators provide unbiased measurements if the blood spectrum is symmetric but partially undersampled [25]. Let us examine the influence of noise for the simple case illustrated in Fig. 4 for bandpass white Gaussian noise (WGN) and a narrow-band Doppler signal. Estimating f_{mean} from the first spectral moment

$$\hat{f}_{\mathrm{mean}} = \frac{f_{\mathrm{PRF}}}{N}\frac{\sum_{i=-N/2}^{N/2} i\,(P_S[i]+P_N[i])}{\sum_{i=-N/2}^{N/2} P_S[i]+P_N[i]} \quad |i| \le \frac{N}{2}$$

we find the estimate is biased low, *viz.*

$$\hat{f}_{\mathrm{mean}} = f_D\frac{\mathrm{SNR}}{1+\mathrm{SNR}}.$$

In this case, SNR is the ratio of the sum of P_S to the sum of P_N. The bias is significant if the SNR is low as it often is for flow imaging below 20 MHz. Additional processing can limit the bias. However, autocorrelator-based estimates are unbiased by additive WGN because the autocorrelation function of the noise at lag one is zero [26]. Clutter filters will affect estimation errors regardless of the estimator.

Zrnic used perturbation analysis to derive the variance of the estimated mean velocity of $N-1$ pulse pairs [24]. He found that for a narrow spectral width and low SNR, the variance is minimal for uniformly spaced sample pairs that share a common sample. Since the echo SNR for blood is low at frequencies below 20 MHz, the method implemented in (5) is optimal for our

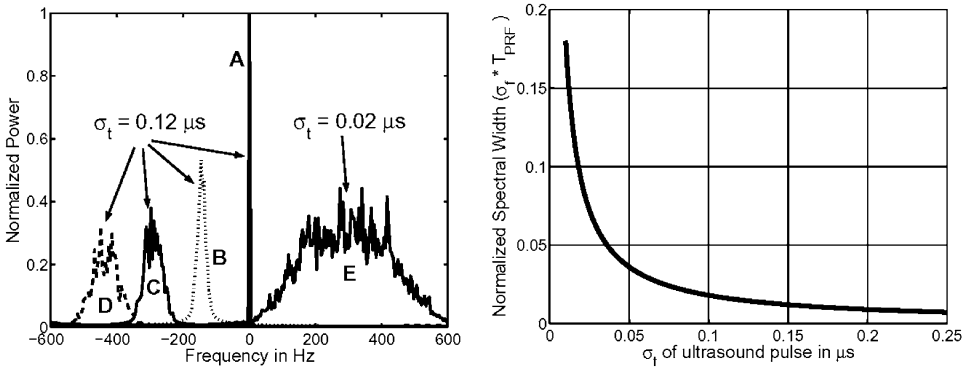

Fig. 5. Left: Spectral broadening as a function of increasing Doppler frequency for four different blood velocities and as a function of ultrasound pulse duration σ_t. The width of spectrum A (zero velocity) indicates that the broadening introduced by the finite window length is negligible. Right: Normalized Doppler spectrum width as a function of Gaussian pulse duration σ_t.

application. The velocity variance $\sigma_{\hat{v}}^2$ of correlated pulse pairs embedded in WGN and for large N is given by [27]

$$\sigma_{\hat{v}}^2 = \frac{c^2}{32\pi^2 T_{\mathrm{PRF}}^2 \rho^2(T_{\mathrm{PRF}}) f_0^2 N^2} \cdot \left\{ \left[1-\rho^2(T_{\mathrm{PRF}})\right] \sum_{\ell=-(N-1)}^{N-1} \rho^2(\ell T_{\mathrm{PRF}}) \times (N-|\ell|) + \frac{1}{N\mathrm{SNR}^2} + \frac{2}{N\mathrm{SNR}} \times \left[1+|\rho(2T_{\mathrm{PRF}})|\left(\frac{1}{N}-1\right)\right]\right\} \tag{7}$$

where $\rho(\ell T_{\mathrm{PRF}}) = \hat{R}(0,\ell)/\hat{R}(0,0)$ is the (complex) echo autocorrelation coefficient at lag ℓ. The dependence of $\sigma_{\hat{v}}^2$ on various parameters is obvious from (7) except perhaps for the dependence on Doppler spectrum width via $\rho(T_{\mathrm{PRF}})$. Spectral width is a function of system parameters, such as beam and pulse widths, and parameters that describe the distribution of RBC density and velocity within the sample volume. Since the envelope of the pulse-echo impulse response is often Gaussian, a Gaussian Doppler power spectrum of width σ_{f_D} is modeled. The Doppler bandwidth depends on many factors. However, if the velocity is constant over time and the range gate is small so that the transit time effect [28] is appropriately expressed by the pulse duration, only pulse parameters and velocity magnitude determine spectral width. For Gaussian-shaped ultrasound pulses of duration parameterized by σ_t, the width of the Doppler power spectrum can be found from

$$\sigma_{f_D} = \frac{1}{\sqrt{2}2\pi\sigma_t}\frac{f_D}{f_0} = \frac{1}{\sqrt{2}2\pi\sigma_t}\frac{2v}{c}. \tag{8}$$

Fig. 5 shows average Doppler power spectra from time-steady velocity fields with different velocity magnitudes and directions as well as different σ_t (computed from 64 simulated IQ signals where $N = 256$.) Doppler spectra A through E show the increase in spectral width with blood velocity for a 15 MHz pulse of width $\sigma_t = 0.12$ μs. Spectrum E originates from a scatterer field that is moving uniformly with a speed equal to that of spectrum C but in the opposite direction and with a larger pulse bandwidth, $\sim 1/\sigma_t$. The shorter pulse ($\sigma_t = 0.02$ μs) increases the spectral width by a factor of 6 compared to spectrum C, and reduces velocity measurement precision because $\sigma_{\hat{v}}^2$ is inversely related to the width of the Doppler spectrum.

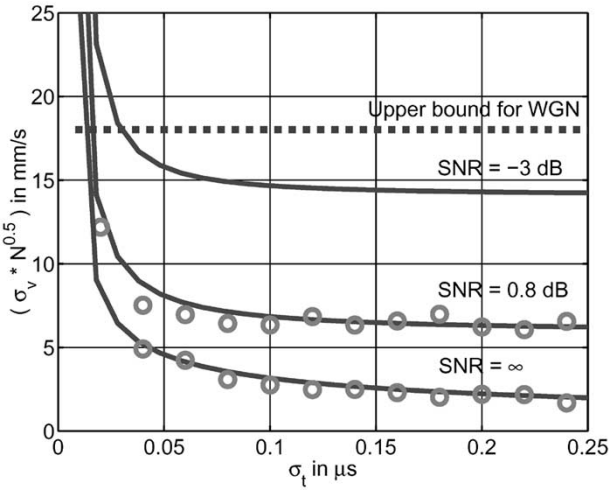

Fig. 6. Comparison of measured (circles) and predicted [solid lines, (9)] velocity variances ($v = 15$ mm/s, $f_0 = 15$ MHz, $T_{\mathrm{PRF}} = 1/1200$ s, $N = 128$, SNR $= \infty$, 0.8 dB, and -3 dB). Equation (9) is valid where it is less than the upper bound.

A reasonable approximation to (7) for Gaussian spectra is [27]

$$\sigma_{\hat{v}}^2 \simeq \frac{c^2}{32\pi^2 T_{\mathrm{PRF}}^2 \rho^2(T_{\mathrm{PRF}}) f_0^2 N} \cdot \left\{ 2\pi^{3/2}\sigma_f T_{\mathrm{PRF}} + \frac{1}{\mathrm{SNR}^2} + \frac{2}{\mathrm{SNR}} \times \left[1-|\rho(2T_{\mathrm{PRF}})|\right]\right\}. \tag{9}$$

The standard deviations measured using simulated echo data are compared to those predicted by (9) in Fig. 6. These results are valid for large N and moderate to high SNR. The variance increases monotonically with decreasing SNR until it reaches the upper bound, $f_{\mathrm{PRF}}^2/12$, equal to the variance for a uniform random variable over the frequency range. Thus, oversampling (excessive f_{PRF}) increases the estimation variance when the

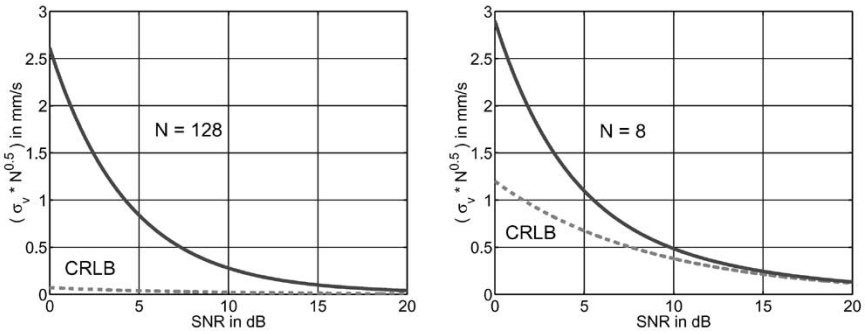

Fig. 7. Complex sinusoid in WGN: autocorrelator velocity standard deviation (solid lines) and CRLB for $N = 128$ (left) and $N = 8$ (right) as functions of SNR ($v = 15$ mm/s, $f_0 = 15$ MHz, and $T_{\rm PRF} = 1/1200$ s).

SNR is low. However, at higher SNR an increase in PRF improves the correlation between samples which results in better estimates. Furthermore, the autocorrelator measures phase from which velocity is computed. For any given error in phase, the error in velocity is reduced for a smaller PRF. So the influence of PRF and pulse duration (which determine the relative Doppler spectrum width) is quite complex, although the optimum PRF that minimizes the estimation variance given in (9) is described in Appendix.

Comparing the autocorrelator variance with the approximate Cramér–Rao lower bound (CRLB) for correlated samples at the optimum PRF shows that the measured variance is twice the lower bound at low SNR [see (13) and (17)]. At high SNR and for $\sigma_{f_D} \cdot T_{\rm PRF} = 0.1$, a ratio of about 10 can be found from (14) and (16). More efficient estimators may exist in low noise situations, e.g., the 2-D autocorrelator described below, but for high noise the 1-D autocorrelator is reasonably efficient.

The literature often uses the CRLB result for pure sinusoids in WGN ($\sigma_t \to \infty$ in Fig. 6). Fig. 7 compares these results with the autocorrelator variance derived from (18) and (19) in the Appendix. For large N and small SNR the autocorrelator variance is significantly higher than the CRLB (Fig. 7, left). This difference diminishes with increasing SNR. When increasing the bandwidth ($\sigma_t < \infty$) we find the opposite is true even for moderate spectral widths. Please note that the CRLB is proportional to N^{-3} whereas the result that bounds the autocorrelator variance decreases with N^{-1} (Fig. 7, right). Therefore, the single frequency CRLB often quoted does not provide guidance for designing CF experiments.

B. Two-Dimensional (2-D) Autocorrelator

The 1-D autocorrelator described in Section III-A is implemented in the vast majority of commercial scanners. It can easily be improved without sacrificing its real-time feature. For example, broadband pulses required for high spatial resolution couple with the frequency-dependent attenuation in tissues to bias velocity estimates. The bias is large when the down-shift in mean radio frequency (MRF) caused by tissue attenuation is significant compared with the Doppler shift produced by slow blood flow. Blood flow close to the skin surface appears very different from that a few centimeters below the surface because the 1-D autocorrelator assumes the mean radio-frequency is constant. To minimize this significant source of velocity bias, the estimator must be capable of tracking frequency shifts caused by blood velocity independently from those of attenuation.

The 2-D autocorrelator is designed to accomplish just that with its ability to estimate both the mean Doppler frequency and MRF within each range gate. The estimator is 2-D in the sense that echo data are processed in both the slow-time and fast-time dimensions (see Fig. 3). When analyzed in two dimensions, a full evaluation of the classic Doppler equation is possible. Also, the center frequency of the transducer needs not be known or measured beforehand so that spectral changes over time, e.g., those with transducer temperature, do not influence estimator performance.

The 2-D autocorrelator provides consistently higher velocity precision than the 1-D autocorrelator under all conditions [31]. However, the superiority of the 2-D autocorrelator is diminished when the velocity spread inside the range gate is large or the echo SNR is low. Both weaken the correlation between Doppler and RF frequency fluctuations that is necessary to improve precision. Loupas [31] found that the crosscorrelator and 2-D autocorrelator velocity estimators offer similar performance at high echo SNR conditions but the latter was noticeably more robust at low SNR. In this study, we apply the 2-D autocorrelator to baseband IQ echo signals. Our system processes analytic signals instead of IQ signals to take advantage of the greater estimation performance in other imaging situations where the echo SNR is large [32].

The axial component of the velocity vector $v_{z_{2D}}$ can be estimated using the same 2-D autocorrelation function of (6) but now taking advantage of the full 2-D information. We estimate $\hat{R}(k,\ell)$ at lags $(k,\ell) = (0,1)$ and $(k,\ell) = (1,0)$ to find [31]

$$v_{z_{2D}} = \frac{\frac{c}{2}\frac{f_{\rm PRF}}{2\pi}\arctan\left(\frac{\Im[\hat{R}(0,1)]}{\Re[\hat{R}(0,1)]}\right)}{f_{\rm dcm} + \frac{f_s}{2\pi}\arctan\left(\frac{\Im[\hat{R}(0,1)]}{\Re[\hat{R}(0,1)]}\right)}, \qquad (10)$$

where $f_{\rm dcm}$ is the demodulation frequency used for quadrature downmixing.

To demonstrate the superior performance of (10) over (5), we generated a linear frequency modulated waveform (chirp) with exponential decay of the form rect $((t - t_p/2)/t_p)\exp(j(f_0 - bt)t)\exp(-\alpha_1 f z)$, where the pulse length is $t_p = 32.5$ μs, the frequency down-shift rate is $b = 0.123$ MHz/μs, and the linear attenuation coefficient, $\alpha(f) = \alpha_1 f$, has the slope $\alpha_1 = 0.593$ dB-cm^{-1}MHz^{-1}/20 $\log_{10} e = 0.068$ cm^{-1}MHz^{-1}. This decaying chirp wave-

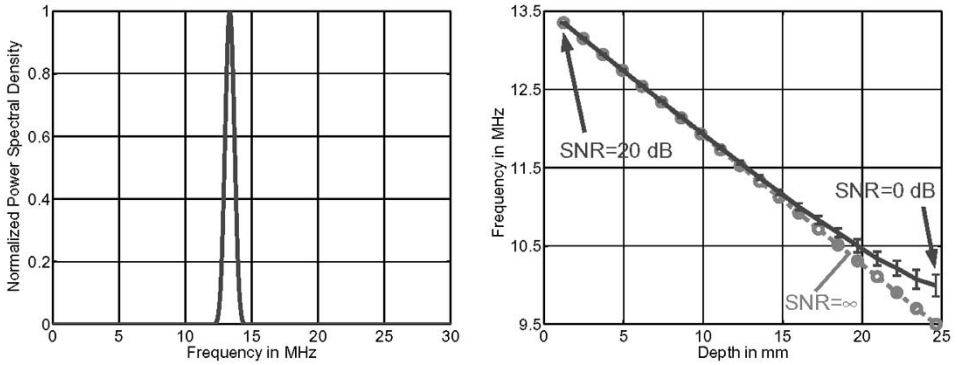

Fig. 8. Denominator of (10) was used to track the MRF of a chirp waveform in additive WGN. On the left is the normalized frequency spectrum at depth $z = 0$ $(t = 0)$ where $f_0 = 13.5$ MHz. The spectral shape is dominated by the range gate. On the right are MRF plots of the estimated (mean ± 1 standard deviation) without noise (SNR $= \infty$) and with noise (20 dB $\geq$ SNR ≥ 0 dB).

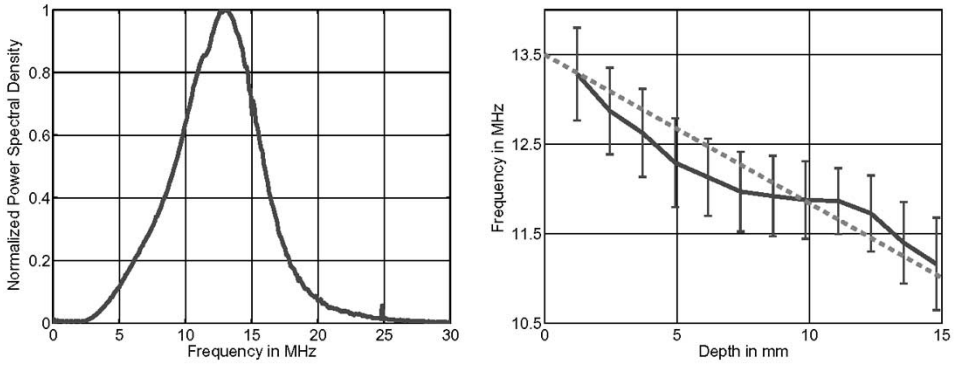

Fig. 9. Denominator of (10) was used to track the MRF for our phantom echo measurements at 13.5 MHz. On the left is the pulse-echo frequency spectrum from a plexiglas plate in water averaged over 500 pulses. On the right are measured center frequency downshift and standard deviation when transmitting pulses with power spectrum shown on the left. The dashed line are values predicted by (11).

form greatly simplifies the effects on the echo spectrum of frequency-dependent attenuation but with realistic tissue parameters. We estimated the MRF of the chirp with and without additive WGN using a rectangular-shaped range with a gate length of 200 samples (1.23 mm), where the waveform is sampled at 125 MS/s, and plotted the results in Fig. 8. Range time is converted to depth via $z = \mathrm{ct}/2$ where $c = 1.54$ mm/μs, the average value in soft biological tissues. With added noise, the maximum SNR at zero depth (first range gate) is approximately 20 dB and the minimum SNR at 25-mm depth (last range gate) is 0 dB. The estimates of mean frequency and standard deviation are computed from superpositions of the chirp with 100 independent noise realizations. We found that bias and variance increase at greater depth where the echo SNR is lower. Reducing the range gate to 50 samples (not shown) increased the estimation variance without affecting bias.

We conducted an experiment analogous to the simulation above with a standard tissue-like graphite-gelatin phantom [33] and our broadband system at 13.5 MHz. Twenty-four echo data sets, each comprising $N = 8$ waveforms, were recorded at independent spatial locations. Estimates of MRF using the denominator of (10) gave the mean ± 1 standard deviation computed for 200 sample range gates ($f_s = 125$ MS/s) that are shown in Fig. 9, right. The downward trend in MRF from frequency-dependent attenuation is clearly seen.

Narrow-band attenuation coefficients were estimated for the phantom at eight frequencies between 2.5 MHz and 11 MHz. Adopting a linear frequency dependence model, we measured $\alpha_1 = 0.498$ dB-cm^{-1}MHz$^{-1}/20 \log e = 0.057$ cm^{-1}MHz^{-1}. At the same frequencies we found $c = 1532 \pm 1$ m/s.

Modeling the pulse-echo impulse response as a Gaussian modulated sinusoid that is attenuated with depth (see Fig. 9, left), the magnitude of the frequency spectrum is $\exp(-2\pi^2(f - f_0)^2\sigma_t^2)\exp(-\alpha_0 f z)$. Combining the exponents and completing the square we find that MRF varies with depth according to

$$\mathrm{MRF} = f_0 - \alpha_1 \frac{B^2}{2} f_0^2 z. \tag{11}$$

The measured fractional bandwidth, $B = 2\sigma_f/f_0$ is 0.566, and the unattenuated center frequency f_0 equals 13.5 MHz. The equation above and the data both predict that the MRF decreases 2.5 MHz for $z = 15$ mm depth. Deviations from linear frequency dependence due to the tissue material and a non Gaussian-shaped pulse spectrum as well as a reduced echo SNR with depth contribute to the nonlinear decrease in measured MRF values seen in Fig. 9.

Ignoring the effects of attenuation, the 2-D autocorrelator is able to provide much lower velocity variance. To compare precision, we applied the 1-D and 2-D autocorrelators to simulated IQ echo data and found the results in Fig. 10. With a packet size of N = 8, we simulated 1000 independent waveform packets where the blood velocity was constant throughout the field and the attenuation was negligible. Each waveform packet was divided into 100 range gates so that error estimates were obtained from

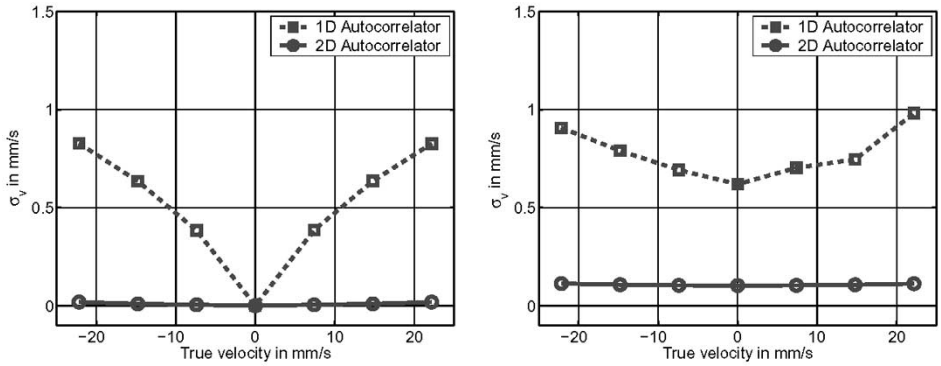

Fig. 10. Comparison of 1-D and 2-D autocorrelators. On the left, the velocity standard deviation σ_v is plotted versus true object velocity for SNR $= \infty$. On the right, the velocity standard deviation is plotted for SNR $= 10$ dB. The aliasing velocity is 30 mm/s and packet size $N = 8$.

$7 \cdot 10^5$ measurements of velocity. The range gate length was selected to match the -20 dB duration of the Gaussian-shaped pulses (0.512 μs or 64 samples at $f_s = 125$ MS/s) with $f_0 = 15$ MHz. The figure shows velocity errors for SNR $= \infty$ and 10 dB. Clearly, the standard deviation of the 2-D autocorrelator estimates is much lower than for the 1-D autocorrelator. Bias errors (not shown) for both estimators are negligible. The estimation precision advantage of the 2-D autocorrelator is greater when fluctuations in the numerator and denominator of (10) are correlated. A high SNR increases correlation between adjacent echo signals in the packet and thus improves the velocity precision of the 2-D autocorrelator. As opposed to the 1-D autocorrelator which is reasonably efficient only at low SNR, the 2-D autocorrelator thus approaches the CRLB at low and high SNR. We also investigated the influences of pulse length, SNR, range gate length and packet size in great detail. Results can be found in [32].

C. Power Doppler

Power Doppler (PD) ultrasonic imaging is valuable for visualizing slow blood flow in solid tissues, such as breast tumors [34]. In CF imaging discussed above, the mean Doppler frequency in each range gate is displayed, whereas in PD imaging the integrated power of the Doppler spectrum is displayed. The power in the Doppler-shifted signal is determined by a coherent summation of echoes from moving scatterers per pulse volume. PD images are much less dependent on Doppler angle than CF imaging, enabling visualization of slow speed and spatially disorganized blood flow even at Doppler angles close to 90°. PD signals are unaffected by aliasing, yet are still limited by noise and clutter. Unlike CF imaging, where the velocity signal is seen to vary significantly throughout the cardiac cycle (time-resolution), the PD signal indicates only the volume of moving RBCs, which is valuable diagnostic information for tumor evaluation.

The variance of power estimates at a fixed position in the body has at least two sources: speckle and additive noise. Ignoring additive noise for the moment and focusing only on speckle noise, the standard deviation of echo power estimates equals the mean value [35] since blood scattering is considered a fully developed speckle condition. Thus, it is necessary to average PD estimates over the packet ensemble size N and/or depth samples to reduce speckle noise. Averaging over the packet ensemble rather than range positions maintains spatial resolution but reduces frame rate. If we were able to average N statistically uncorrelated power samples, the variance of the mean power would be reduced by the factor $1/N$ when compared to the variance of a single sample. However, power samples in the ensemble are always correlated, particularly for slow flow, so the variance reduction factor $1/N_E$ is given by (for a stationary process and equally spaced samples) [36]

$$N_E^{-1} = \sum_{n=-(N-1)}^{N-1} \frac{N-|n|}{N^2} \rho_P(nT_{\mathrm{PRF}}) \tag{12}$$

where $\rho_P(nT_{\mathrm{PRF}})$ is the (real) autocorrelation coefficient for power samples. Broadband pulses and focused beams yield PD estimates with short correlation lengths, which provide many uncorrelated samples in the ensemble for efficient averaging. Thus, speckle noise in broadband PD images is reduced without compromising spatial resolution and with only a modest loss of frame rate. Unlike CF images, broadband pulse transmission is desired for low speckle-noise PD imaging.

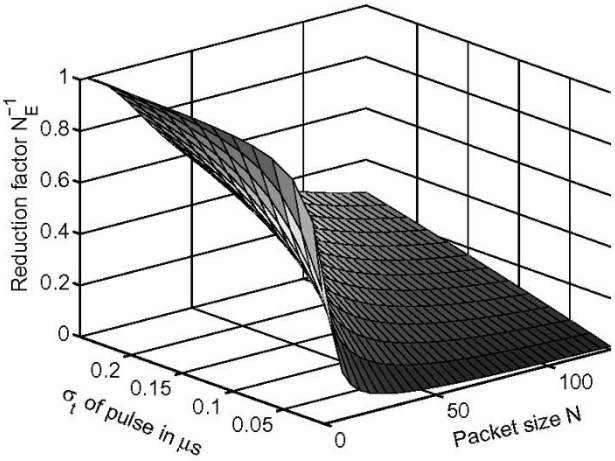

Fig. 11. Variance reduction factor N_E^{-1} as a function of the number of estimates in the range gate N and Gaussian pulse duration σ_t. A time-steady velocity field of 15 mm/s is probed at a PRF of 1200 Hz. A value of 1 indicates the standard deviation of the estimated mean power equals the signal mean power, and, therefore, no reduction in estimation variance is achieved.

For example, assume a Gaussian-shaped pulse envelope of duration σ_t. Squaring and then autocorrelating the result we find $\exp(-t^2/2\sigma_t^2)$. From (8) that relates σ_{f_D} to σ_t, we write $\rho_P(nT_{\mathrm{PRF}}) = \exp(-4\pi^2\sigma_{f_D}^2 n^2 T_{\mathrm{PRF}}^2)$. Applying this function to (12), we compute and plot the results in Fig. 11 to view the

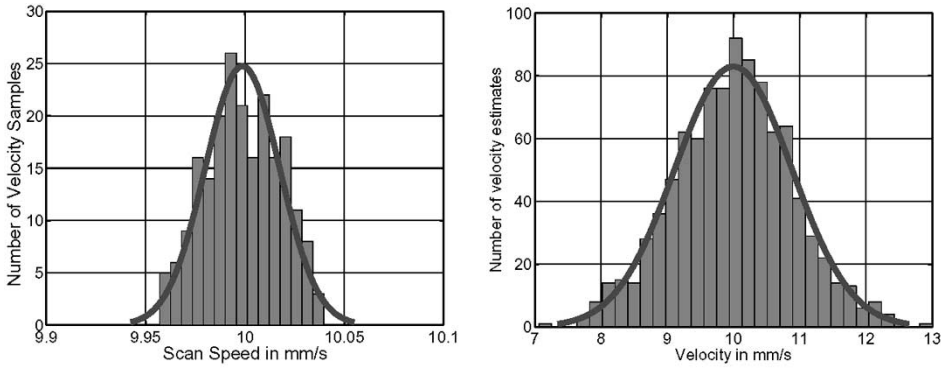

Fig. 12. Histograms and Gaussian fits of scan speed (left) and measured velocity (right). Note the difference in scales. The mean and standard deviation of the scan speed are 9.9987 mm/s and 0.0187 mm/s. The mean and standard deviation of the measured velocity are 10.051 mm/s and 0.6674 mm/s.

variance reduction factor N_E^{-1} as a function of σ_t and packet size N.

The data in Fig. 11 are valid assuming a uniform blood velocity to be consistent with the assumption of stationarity used to derive (12). Tortuous or turbulent flows are not examples of stationary random processes, so (12) does not apply in complex flow situations. However, ideal tumor flow conditions are those that yield increased Doppler power not eliminated by the wall filter and rapidly decorrelating echoes within the ensemble packet. The high ensemble echo correlation necessary for CF imaging is detrimental for PD imaging.

Since additive noise is uncorrelated between packet ensemble waveforms, it is greatly reduced by averaging. However, increasing the bandwidth of transmitted pulses decreases the echo SNR and diminishes the beneficial effects of broadband transmission. As long as speckle dominates over noise variance, broadband pulses are beneficial. The best design strategy for PD tumor imaging includes highly focused, broadband, low-noise systems, perhaps enhanced with a low concentration of contrast media.

IV. Experimental Results

Two experiments were performed to assess the overall velocity estimation accuracy and precision of our system. The first experiment examines performance for constant velocity flow while the second examines performance for spatially varying velocity requiring spatial resolution.

A. Measurement Accuracy for Constant Velocity

A solid graphite-gelatin phantom with a rectangular shape was placed in a water-alcohol solution with matching sound speed and scanned with the system illustrated in Fig. 1. The transducer was tipped in the yz-scan plane by the angle $\varphi = 15°$. Acquiring echo data while translating the transducer at a constant speed of 10 mm/s parallel to the phantom top surface, we generated known constant flow conditions at a Doppler angle of $\theta = 75°$. The polarity of the velocity depends on the scan direction.

RF echo signals were recorded at 125 MS/s within the depth-of-focus centered at a phantom depth of 20 mm using a 15 MHz, f/3.54 spherically focused transducer. The scan speed, which determines the Doppler shift and object velocity, was obtained 210 times by using the motion controller and optical quadrature encoder readings. A histogram is shown in Fig. 12, left. The mean speed is highly accurate and precise $(9.9987 \pm 0.0013\ \mathrm{mm/s})$ and represents the reference for the ultrasonic velocity measurements.

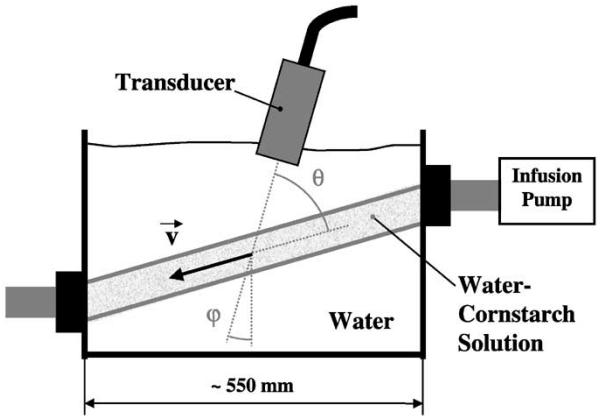

Fig. 13. Experiment to measure parabolic flow profiles. In this case, refraction at the tube wall does not influence the measurement.

The 2-D autocorrelator was applied to eight-fold-decimated IQ signals (64 LOS, $N = 8$) in order to verify its estimation performance. We computed 6720 velocity estimates from 0.6-mm range gates (matched to the -20 dB pulse duration) at 960 independent spatial locations while scanning the phantom. The angle-corrected mean and standard deviation of the estimated velocity are 10.051 and 0.667 mm/s (Fig. 12, right). The measurement bias is just 0.5% of the mean scan speed which proves that the 2-D autocorrelator provides accurate velocity estimates. We calculated a generous upper bound for the standard deviation of the measured mean velocity by assuming only 960 of the 6720 estimates were uncorrelated and found $0.6674/\sqrt{960} = 0.022\ \mathrm{mm/s}$. The standard error is less than 0.2% of the mean estimate. Thus, the 2-D autocorrelator is also fairly precise even for relatively slow velocity.

B. Measurement Accuracy for Spatially Varying Velocity

Velocity bias and variance were also determined from estimates acquired in a circular flow channel phantom (Fig. 13). A known flow profile was generated in a straight tube with constant cross-sectional diameter and laminar, fully developed, steady Poiseuille flow of Newtonian character. To create such flow, we determined the "entry length" from the mouth of the

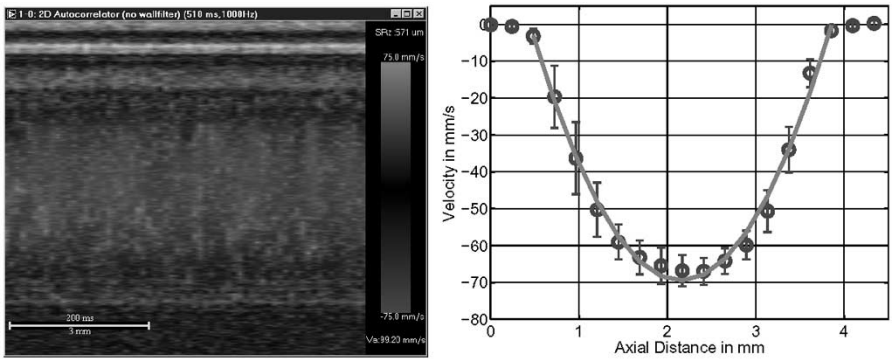

Fig. 14. Left: Color M-mode image for steady Poiseuille flow. The horizontal axis covers 512 ms of time and the velocity resolution in depth is 0.245 mm. The bar in the lower left corner represents 200 ms and 3 mm, respectively. Right: Time-averaged velocity profile including standard deviations and a parabolic fit. Error bars indicate ± 1 standard deviation of a single line profile.

tube after which the flow becomes fully developed. If a fluid with density ρ and viscosity μ enters the tube of diameter d with constant velocity u (blunt flow entry), the centerline velocity downstream in the tube reaches 99% of its Poiseuille flow value after the entry length [37]

$$l_e = 0.04\, d\mathrm{Re} = \frac{0.04 d^2 \rho u}{\mu},$$

where Re is the Reynolds number. In our experiment, $\mathrm{Re} \simeq 100$ giving an entry length of $4d$.

An M-mode experiment to measure 1-D flow velocity profiles across the flow channel is diagrammed in Fig. 13. A latex rubber flow tube with 3.4 ± 0.1 mm inner diameter was mounted at an angle of $16^\circ \pm 1^\circ$ from horizontal in a plexiglass tank filled with distilled water at 22°C. The tube was stretched slightly for stability such that its outer diameter decreased from 5 mm to 4.85 mm. A variable-rate infusion pump (SAGE, M362, flow accuracy $\pm 4\%$ of setting) fed the tube a 1% by mass water-cornstarch suspension (22°C, $c = 1488$ m/s) at a rate 17.5 ± 0.7 ml/min. We estimated the inner diameter of the tube by measuring the distance between zero-velocity regions from the flow profile and a very short range gate length. That gave an inner tube diameter of 3.3 mm. Steady Poiseuille flow in a 3.3-mm-diameter tube at a rate given above has a peak velocity of 68.2 ± 2.73 mm/s. The transducer probed the tube 250 mm from the flow entrance, therefore a parabolic flow profile was expected.

Accurate velocity measurements in a flow gradient situation require an ultrasonic pulse volume with dimensions much smaller than the tube diameter. We used a spherically focused, 7.5 MHz, f/1.33 transducer with a beam width BW $=$ 0.267 mm, and a depth-of-focus DOF $=$ ± 1.2 mm about the radius of curvature. The transducer was tilted by $\varphi = 15^\circ$ from vertical so that the Doppler angle was $\theta = 59^\circ \pm 1^\circ$. The relative velocity error $\Delta v/v = (\sin\theta/\cos\theta)\Delta\theta$ due to the uncertainty $\Delta\theta$ in the Doppler angle was found by error propagation to be $\pm 2.9\%$.

RF echo signals were acquired at 125 MS/s over a time period of 512 ms at $f_{\mathrm{PRF}} = 1$ kHz (aliasing velocity is approx. 96 mm/s). Velocities were estimated from 8-fold decimated IQ signal packets $(N = 8)$ using the 2-D autocorrelator. Six-sample (decimated) range gates gave a corresponding RGL in beam direction of 0.286 mm which corresponds to 0.245 mm cross-sectional length after taking the geometry of the setup into account. The color M-mode image and time-averaged flow profile are shown in Fig. 14. Error bars on the right side of the profile are smaller than on the left because the density of the cornstarch scatterers caused them to settle more in the bottom half of the tube. Varying error demonstrates that echo SNR is an important factor determining velocity variance. The excellent fit of the measured profile to the parabola and the close agreement of the measured and predicted peak velocities show velocity measurements in flow gradients are unbiased.

V. Conclusion

Our 10–15 MHz flow imaging system, designed for color-flow (CF) and power-Doppler (PD) imaging, has sufficient sensitivity, precision, and accuracy to visualize blood flow in tumors under ideal conditions. Questions of practicality are answered by relating the geometry of a specific flow field to the spatial resolution and echo contrast of the system. The best strategies for imaging tumor flow select the ultrasonic pulse volume that maximizes the net RBC velocity vector. A larger pulse volume (lower spatial resolution) detects more moving blood volume and increases the echo SNR if the motion of individual RBCs is coordinated. In the tortuous, randomly-oriented vasculature common in tumors, the net velocity vector is reduced for large pulse volumes. Consequently, the lowest velocity errors are produced at a spatial resolution optimized for specific imaging situations.

Tumor vessels are mostly capillaries roughly 4–10 μm in diameter and separated on average by 20–50 μm. The latter value is based on knowledge that oxygen diffuses in tissue only 120 μm. It is not possible to spatially resolve this flow structure noninvasively at ultrasonic frequencies below 20 MHz. The most promising Doppler-based approach to visualizing the presence of blood flow is broadband PD imaging. PD imaging is most precise at high spatial resolution if clutter and noise can be minimized.

CF imaging adds information about directionality and time resolution during the cardiac cycle. However, flow heterogeneity and the low scattering of RBCs severely limit velocity estimation. The ideal strategy for real-time CF imaging of tumors is to apply the 2-D autocorrelator to echo signals having a bandwidth adjusted to optimize the interpacket echo

correlation. Under these conditions and for Gaussian-shaped Doppler spectra, velocity estimation is efficient in that estimation variance approaches the CRLB. A low concentration of contrast media improves CF and PD imaging of tumors by increasing the echo SNR.

APPENDIX

The value of T_{PRF} that minimizes the autocorrelator's estimation variance can be found from (9) for low SNR to be $(\sqrt{2}\cdot 2\pi\sigma_{f_D})^{-1}$ which gives a corresponding minimum variance of [27]

$$\sigma_{\hat{v}}^2 \approx \frac{c^2\sigma_{f_D}\sqrt{2\exp(1)}}{16\pi T_{\mathrm{PRF}} f_0^2 N}\frac{1}{\mathrm{SNR}^2}. \tag{13}$$

At large SNR and narrow Gaussian spectra (9) can be approximated by

$$\sigma_{\hat{v}}^2 \approx \frac{c^2\sigma_{f_D}}{16\sqrt{\pi}T_{\mathrm{PRF}} f_0^2 N}. \tag{14}$$

In order to compare the estimation performance of the autocorrelator with the optimum estimator it is necessary to know the minimum variance bound. CRLBs specify the lowest variance of any unbiased estimate. If samples are correlated, as in CF imaging, it is difficult to exactly solve the likelihood equations and derive the CRLB (and the optimum maximum-likelihood estimator which asymptotically approaches the CRLB [29]). Approximate CRLBs for correlated samples with Gaussian-shaped spectra embedded in WGN are given in [27] for small SNR

$$\sigma_{\hat{v}}^2 \geq \frac{1}{T_{\mathrm{PRF}}^2 N}\frac{\sqrt{\pi}(\sigma_{f_D}T_{\mathrm{PRF}})^3}{\mathrm{SNR}^2}\frac{c^2}{f_0^2}, \tag{15}$$

and large SNR

$$\sigma_{\hat{v}}^2 \geq \frac{1}{T_{\mathrm{PRF}}^2 N}\frac{3(\sigma_{f_D}T_{\mathrm{PRF}})^4}{1-12(\sigma_{f_D}T_{\mathrm{PRF}})^2}\frac{c^2}{f_0^2}. \tag{16}$$

To make a comparison with (13) straightforward, (15) can be rewritten using the optimum value of $T_{\mathrm{PRF}} = (\sqrt{2}\cdot 2\pi\sigma_{f_D})^{-1}$ which minimizes the autocorrelator variance

$$\sigma_{\hat{v}}^2 \approx \frac{c^2\sigma_{f_D}\pi^{-3/2}}{8T_{\mathrm{PRF}} f_0^2 N}\frac{1}{\mathrm{SNR}^2}. \tag{17}$$

An exact solution of the likelihood equations is possible for a finite number of discrete-time observations of a complex sinusoid embedded in WGN. From the Fisher information matrix, the CRLB of the frequency f is [30]

$$\sigma_{\hat{f}}^2 \geq \frac{6}{4\pi^2 T_{\mathrm{PRF}}^2 N^2(N-1)\mathrm{SNR}} \tag{18}$$

and serves as reference to compare with the variance obtained from the autocorrelator when estimating a complex sinusoid in WGN [24]

$$\sigma_{\hat{f}}^2 = \frac{1}{8\pi^2 T_{\mathrm{PRF}}^2 N\mathrm{SNR}}\left(\frac{2}{N}+\frac{1}{\mathrm{SNR}}\right). \tag{19}$$

ACKNOWLEDGMENT

The authors would like to thank D. Kruse for guidance and advice regarding the design and construction of the instrumentation in its early phases and for his comments on the manuscript. They would also like to thank S. Nicholson for the final proof-reading of the manuscript.

REFERENCES

[1] N. Weidner *et al.*, "Tumor angiogenesis: A new significant and independent prognostic indicator in early-stage breast carcinoma," *J. Nat. Cancer Inst.*, vol. 84, pp. 1875–87, 1992.
[2] N. Weidner, "Tumoural vascularity as a prognostic factor in cancer patients: The evidence continues to grow," *J. Pathol.*, vol. 184, pp. 119–122, 1998.
[3] K. Axelsson *et al.*, "Tumor angiogenesis as a prognostic assay for invasive ductal breast carcinoma," *J. Nat. Cancer Inst.*, vol. 87, pp. 997–1008, 1995.
[4] A. Vincent-Salomon *et al.*, "Long term outcome of small size invasive breast carcinomas independent from angiogenesis in a series of 685 cases," *Cancer*, vol. 92, pp. 249–256, 2001.
[5] A. J. Guidi *et al.*, "Association of angiogenesis in lymph node metastases with outcome of breast cancer," *J. Nat. Cancer Inst.*, vol. 92, pp. 486–92, 2000.
[6] M. Tozaki *et al.*, "Power Doppler sonogragphy of breast masses: Correlation of doppler spectral parameters with tumor angiogenesis and histologic growth patterns," *J. Ultrasound Med.*, vol. 19, pp. 593–600, 2000.
[7] E. F. Donnelly *et al.*, "Quantified power Doppler US of tumor blood flow correlates with microscopic quantification of tumor blood vessels," *Radiology*, vol. 219, pp. 166–70, 2001.
[8] W. T. Yang *et al.*, "Benign and malignant breast masses and axillary nodes: Evaluation with echo-enhanced color power Doppler US," *Radiology*, vol. 220, pp. 795–802, 2001.
[9] H. S. Mhanna, B. Trummer, Ch. Kargel, and M. F. Insana, "Ultrasonic annular array system for detecting tissue motion," *Proc. SPIE*, vol. 4687, pp. 171–181, 2002.
[10] *IMAQ Vision Manual*, National Instruments, 2000.
[11] D. E. Kruse, R. H. Silverman, R. J. Fornaris, D. J. Coleman, and K. W. Ferrara, "A swept-scanning mode for estimation of blood velocity in the microvasculature," *IEEE Trans. Ultrason., Ferroelect., Freq. Contr.*, vol. 45, pp. 1437–1440, 1998.
[12] J. A. Jensen, *Estimation of Blood Velocities Using Ultrasound. A Signal Processing Approach*. Cambridge, U.K.: Cambridge Univ. Press, 1996.
[13] J. M. Rubin, R. O. Bude, P. Carson, R. L. Bree, and R. S. Adler, "Power Doppler US: A potentially useful alternative to mean frequency-based color Doppler US," *Radiology*, vol. 190, no. 3, pp. 853–856, 1994.
[14] P. Chaturvedi, M. F. Insana, and T. J. Hall, "Testing the limitations of 2-D local companding in strain imaging using phantoms," *IEEE Trans. Ultrason., Ferroelect., Freq. Contr.*, vol. 45, pp. 1022–1031, Oct. 1998.
[15] Ch. Kargel, G. Höbenreich, B. Trummer, and M. F. Insana, "Adaptive clutter rejection filtering in ultrasonic strain-flow imaging," *IEEE Trans. Ultrason., Ferroelect., Freq. Contr.*, vol. 50, pp. 824–835, Aug. 2003.
[16] *Private Communication With Support Engineers From Galil Motion Control* Rocklin, CA, 2001.
[17] J. S. Bendat and A. G. Piersol, *Random Data: Analysis and Measurement Procedures*, 2 ed. New York: Wiley, 1986.
[18] L. A. F. Ledoux, P. J. Brands, and A. P. G. Hoeks, "Reduction of the clutter component of Doppler ultrasound signals based on singular value decomposition: A simulation study," *Ultrason. Imaging*, vol. 19, pp. 1–18, 1997.
[19] A. Bjaerum, H. Torp, and K. Kristoffersen, "Clutter filters adapted to tissue motion in ultrasound color flow imaging," *IEEE Trans. Ultrason., Ferroelect., Freq. Contr.*, vol. 49, pp. 693–704, June 2002.
[20] S. R. Saunders, *Antennas and Propagation for Wireless Communication Systems*. New York, NY: Wiley, 1999.
[21] A. V. Oppenheim and R. W. Schafer, *Discrete Time Signal Processing*, 2 ed. Englewood Cliffs, NJ: Prentice-Hall, 1999.
[22] C. Kasai, K. Namekawa, A. Koyano, and R. Omoto, "Real-time two-dimensional blood flow imaging using an autocorrelation technique," *IEEE Trans. Son. Ultrason.*, vol. SU-32, pp. 458–464, June 1985.
[23] R. Bracewell, *The Fourier Transform and its Applications*. New York: McGraw-Hill, 1965.
[24] D. S. Zrnic, "Estimation of spectral moments for weather echos," *IEEE Trans. Geosci. Electron.*, vol. GE-17, pp. 113–128, Jan. 1979.

[25] R. J. Doviak and D. S. Zrnic, *Doppler Radar and Weather Observations*, 2nd ed. New York: Academic, 1993.
[26] W. D. Barber, J. W. Eberhard, and S. G. Karr, "A new time domain technique for velocity measurements using Doppler ultrasound," *IEEE Trans. Biomed. Eng.*, vol. BME-32, pp. 213–229, Feb. 1985.
[27] D. S. Zrnic, "Spectral moment estimators from correlated pulse pairs," *IEEE Trans. Aero. Electron. Syst.*, vol. AES-13, pp. 344–354, June 1977.
[28] V. L. Newhouse, P. J. Bendick, and L. W. Varner, "Analysis of transit time effects on Doppler flow measurement," *IEEE Trans. Biomed. Eng.*, vol. BME-23, pp. 381–387, Mar. 1976.
[29] H. L. Van Trees, *Detection, Estimation, and Linear Modulation Theory*. New York: Wiley, 1968, pt. I.
[30] D. C. Rife and R. R. Boorstyn, "Single tone parameter estimation from discrete-time observations," *IEEE Trans. Inform. Theory*, vol. IT-20, pp. 591–598, May 1974.
[31] T. Loupas, R. B. Peterson, and R. W. Gill, "Experimental evaluation of velocity and power estimation for ultrasound blood flow imaging, by means of a two-dimensional autocorrelation approach," *IEEE Trans. Ultrason., Ferroelect., Freq. Contr.*, vol. 42, pp. 689–699, Apr., 1995.
[32] G. Plevnik, "Performance Evaluation of Autocorrelation-Based Velocity Estimators for Blood Flow Imaging," M.S. thesis, Graz University of Technology, Graz, Austria, 2002.
[33] J. J. Mai and M. F. Insana, "Strain imaging of internal deformation," *Ultrasound Med. Biol.*, vol. 28, pp. 1475–1484, 2002.
[34] F. Denis *et al.*, "In vivo quantitation of tumour vascularization assessed by Doppler sonography in rat mammory tumours," *Ultrasound Med. Biol.*, vol. 28, pp. 431–437, 2002.
[35] J. W. Goodman, *Statistical Properties of Laser Speckles*. Berlin, Germany: Springer-Verlag, 1975.
[36] F. E. Nathanson, *Radar Design Principles, Signal Processing and the Environment*. New York: McGraw-Hill, 1969.
[37] M. Zamir, *The Physics of Pulsatile Flow*. New York: Springer-Verlag, 2000.

Christian Kargel (M'03) received the B.S. and M.S. degrees (with honors) in electrical engineering (electronics and communications) and the Ph.D. degree (with honors) in coherent optics and statistical signal processing from the Graz University of Technology, Austria.

In 1995, he joined the Department of Electrical Engineering, Graz University of Technology. Until August 2000, he was an Assistant Professor of electrical measurement, measurement signal processing, and instrumentation at the Graz University of Technology. From September 2000 to July 2002, he was a Visiting Assistant Professor in the Department of Biomedical Engineering, University of California, Davis, where his research work was focused mainly on ultrasound-based velocity estimation and strain imaging. Since October 2002, he has been a Professor of medical electronics and instrumentation in the newly-created Department of Medical Information Technology, Carinthia Tech Institute, University of Applied Sciences, Austria. His research interests include medical imaging, electronics, and instrumentation, as well as biomedical signal and optical information processing.

Gernot Plevnik was born in Graz, Austria, in 1976. He received the Dipl.-Ing. degree in electrical engineering from the Graz University of Technology, Austria, in 2002.

In 2001, he did research work for his M.S. thesis at the University of California, Davis, where he worked in the field of color-flow signal processing and system architecture. Since 2003, he has been with the Andritz AG, Austria, working on process simulations.

Birgit Trummer was born in Graz, Austria, in 1971. She received the Dipl.-Ing. degree in electrical engineering (process design) from the Graz University of Technology in 2001. Her thesis was on contactless displacement-measurement using laser speckles.

From 2001 to 2002, she was a Postgraduate Researcher at the Biomedical Engineering Department, University of California, Davis, where she worked on the development of an experimental ultrasonic scanner system. Since 2002 she has been with the EFKON AG, Austria, working in the hardware development team. Her main field of interest is digital signal processing.

Michael F. Insana (M'85) received the Ph.D. degree in medical physics from the University of Wisconsin, Madison, in 1983. His dissertation topic was acoustic scattering and absorption in biological tissues.

He was a research physicist at the FDA from 1984 to 1987, where he developed methods for describing tissue microstructure from the statistical properties of echo signals. From 1987 to 1999, he was with the Department of Radiology, University of Kansas Medical Center. There, he directed an imaging research laboratory that designed and evaluated new ultrasonic imaging methods for studying progressive renal failure and breast cancer. Since 1999, he has been a Professor of biomedical engineering at the University of California, Davis. He is Vice Chair of the department and Chair of the graduate group. His research is the development of novel ultrasonic instrumentation and methods for imaging soft tissue microstructure, elasticity, and blood flow. The goal is to understand basic mechanisms of tumor formation and responses to therapy. His research includes the fundamentals of imaging system design and performance evaluation, signal processing, detection, and estimation.

Dr. Insana is a member of the ASA, a Fellow of the Institute of Physics, and Associate Editor for IEEE TRANSACTIONS ON MEDICAL IMAGING.